ACS Catalysis

pubs.acs.org/acscatalysis

Research Article

Potential-Induced Synthesis and Structural Identification of Oxide-Derived Cu Electrocatalysts for Selective Nitrate Reduction to Ammonia

Na Zhou, Zhi Wang, Ning Zhang, Di Bao,* Haixia Zhong,* and Xinbo Zhang*

Cite This: *ACS Catal.* 2023, 13, 7529–7537

Read Online

ACCESS | Metrics & More | Article Recommendations | Supporting Information

ABSTRACT: Developing effective electrocatalysts for nitrate reduction to ammonia is paramount for ammonia synthesis while addressing the water pollutant issue. Identifying the active structure and its correlation with catalytic behavior during the reaction process is essential and challenging for the rational design of advanced electrocatalysts. Herein, starting from Cu_2O particles with controllable crystal facets, the electrochemically reconstituted Cu/Cu_2O was fabricated as a suitable catalytic system, and the relationship between the chemical state of copper and product selectivity in the nitrate reduction reaction was studied. At −0.9 V versus reversible hydrogen electrode, the oxide-derived Cu^0 (OD-Cu) cube achieved a high ammonia Faradaic efficiency of 93.9% and productivity of up to 219.8 μmol h^{-1} cm^{-2}, surpassing those of most Cu-based catalysts. In situ Raman analysis, well-designed pulsed electrolysis experiments, and theoretical calculations showed that ammonia was preferentially produced on OD-Cu at high reduction potentials and the presence of the Cu/Cu_2O interface favored nitrite formation at low reduction potentials. The high ammonia selectivity of the OD-Cu cube originated from the enhanced adsorption of nitrate and lower reaction barrier of the potential-determining step (*NH_3 → NH_3). This work presents an effective strategy to boost electrocatalysis and offers an insight into the real active phase and corresponding catalytic behavior of Cu-based electrocatalysts.

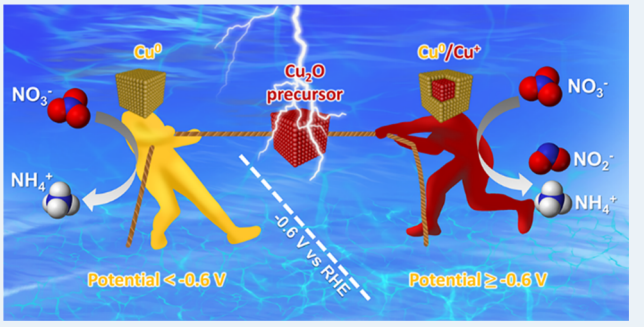

KEYWORDS: *nitrate reduction reaction, oxide-derived copper, ammonia synthesis, in situ Raman, electrochemical reconstruction*

1. INTRODUCTION

Ammonia (NH_3), as an important commodity or energy carrier, is critical to chemical synthesis, fertilizer manufacturing, and renewable energy storage and conversion, greatly impacting the development of modern society.[1−5] Current large-scale NH_3 synthesis still relies heavily on the energy- and capital-intensive Haber−Bosch process, which consumes 2% of the global energy and produces >1% of the global CO_2 emissions.[6,7] Recently, intensive efforts have been devoted to developing a sustainable and eco-friendly alternative for NH_3 production, and the electrochemical nitrogen reduction reaction (NRR) under mild conditions powered by renewable energy sources has attracted extensive attention.[8−11] However, the selectivity and yield of NH_3 produced via the NRR are extremely low because of the low water solubility and high N≡N bond dissociation energy (945 kJ mol^{-1}) of N_2, which are far behind the industrial requirements.[12,13] The electroreduction of nitrate (NO_3^-), which has a high water solubility and low N═O bond dissociation energy (204 kJ mol^{-1}),[14,15] has great potential to produce NH_3 at a faster reaction rate while eliminating NO_3^- pollution in the environment.[16−18] Nevertheless, the NO_3^- reduction reaction (NO_3RR) to NH_3 involves multiple electron and proton transfer processes, which may afford different products including NO_2^-, NO, N_2, and NH_2OH,[19−22] and thus exhibits an unsatisfactory NH_3 selectivity. Therefore, developing a highly efficient and selective catalyst for the NO_3RR to NH_3 is a prerequisite.

Among the various alternatives, Cu-based materials have been extensively studied owing to their large numbers of unpaired d-orbital electrons, moderate energy barriers for intermediate adsorption, and suppression of the hydrogen evolution reaction (HER).[23−25] In recent years, various efficient Cu-based catalysts, such as defect-rich Cu(100),[26] CuBDC@$Ti_3C_2T_x$,[27] Cu@C,[28] Rh@Cu NWs,[29] CuCoSP,[30] and Cu−N−C,[31] have been reported in NO_3RR to NH_3. Particularly, the oxide-derived Cu-based catalyst fabricated via in situ electrochemical reconstruction exhibited an enhanced selectivity of NH_3 during NO_3^- reduction.[32−35] For example,

Received: March 22, 2023
Revised: May 6, 2023

https://doi.org/10.1021/acscatal.3c01315
ACS Catal. 2023, 13, 7529−7537

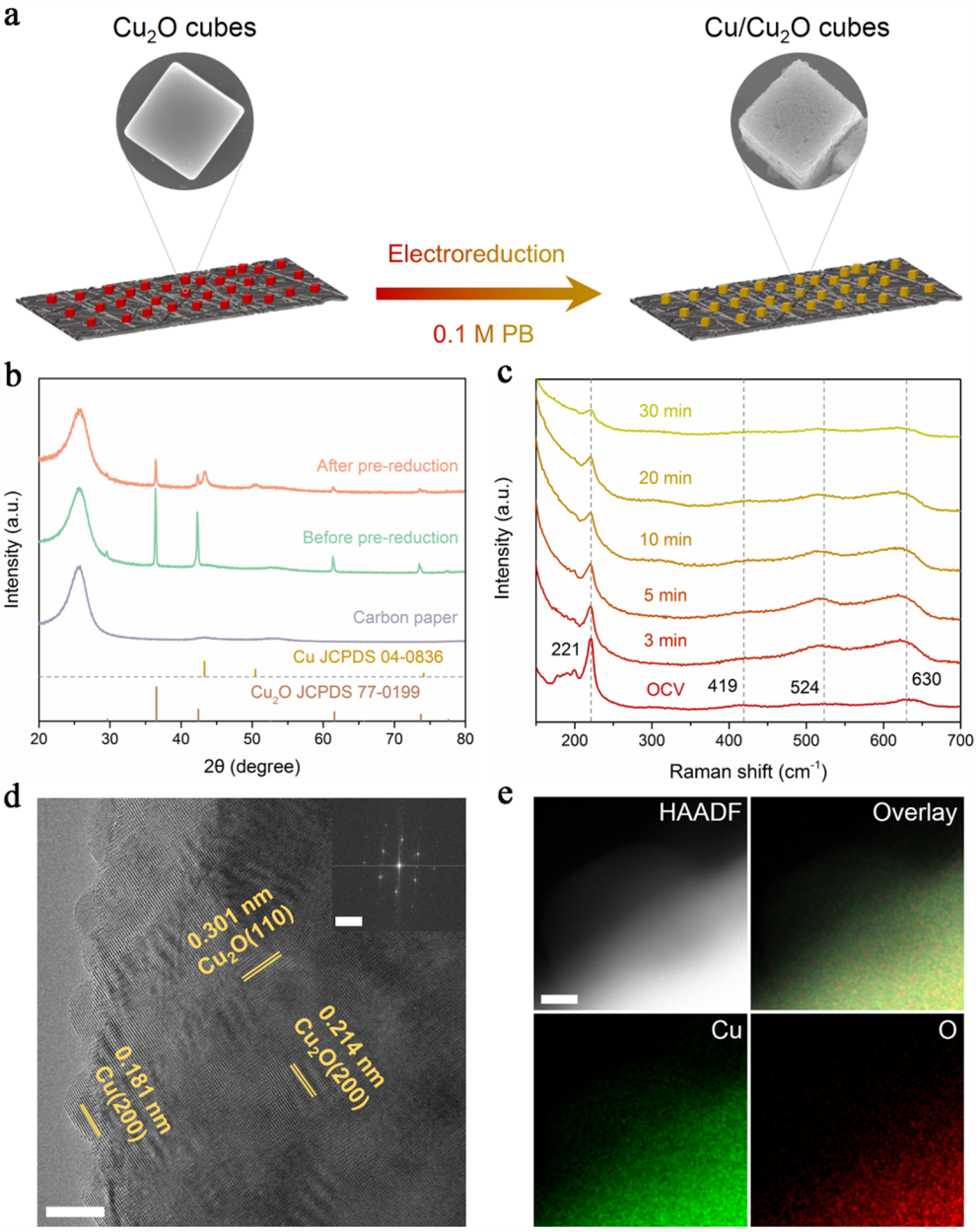

Figure 1. Structural characterization of Cu/Cu_2O interfaces. (a) Schematic illustration of the construction of the stable Cu/Cu_2O interface structure by electrochemical prereduction strategy at −0.6 V vs RHE in 0.1 M PB solution. (b) XRD patterns of Cu_2O cubes before and after prereduction stabilization. (c) In situ Raman spectra collected during the prereduction of Cu_2O cubes. (d) HRTEM characterization of the Cu/Cu_2O interface (inset: the FFT image). (e) STEM image and the corresponding elemental mapping of the distribution for Cu (green) and O (red) at the Cu/Cu_2O interface. Scale bars: 5 nm (d), 5 nm (e), and 5 1/nm for inset in (d).

Zhang's group constructed a Cu/Cu_2O interface as the active phase by in situ reduction of CuO arrays and achieved highly selective NO_3^- reduction to NH_3.[36] Similarly, Ren et al. reported that the thin outer concave-convex oxide layer of the $Cu/Cu_{2+1}O$ interface structure possessed an optimized Cu d-band center and adsorption energies of key intermediates and afforded high catalytic performance.[37] These studies suggest that the improved NH_3 selectivity of the Cu/Cu_2O interface is associated with a reduced energy barrier for NO_3^- reduction to NH_3 on Cu^+ active sites.[19,38] However, the unstable Cu^{2+}/Cu^+ species are in situ electrochemically transferred to Cu^0 during the NO_3^- reduction process, which is claimed as an intrinsically active site.[26,39] Despite these achievements, the real catalytic structure and its relationship with the activity/selectivity of these Cu-based materials remain in disagreement. Monitoring the dynamic structural changes and the corresponding effects on the activity of Cu-based catalysts during the NO_3RR process, such as the oxidation state of Cu, is necessary to develop new advanced electrocatalysts for NO_3^- reduction to NH_3. However, because Cu-based materials are susceptible to oxidation/reduction under working conditions and probing limitations, understanding the true active site and its correlation with the catalytic performance under the realistic working condition is full of challenges.[40,41] In this context, it is necessary to construct a suitable model catalyst system and utilize the advanced in situ characterization.

Herein, starting from Cu_2O particles with controllable crystal facets, a suitable Cu/Cu_2O model catalyst was

https://doi.org/10.1021/acscatal.3c01315
ACS Catal. 2023, 13, 7529−7537

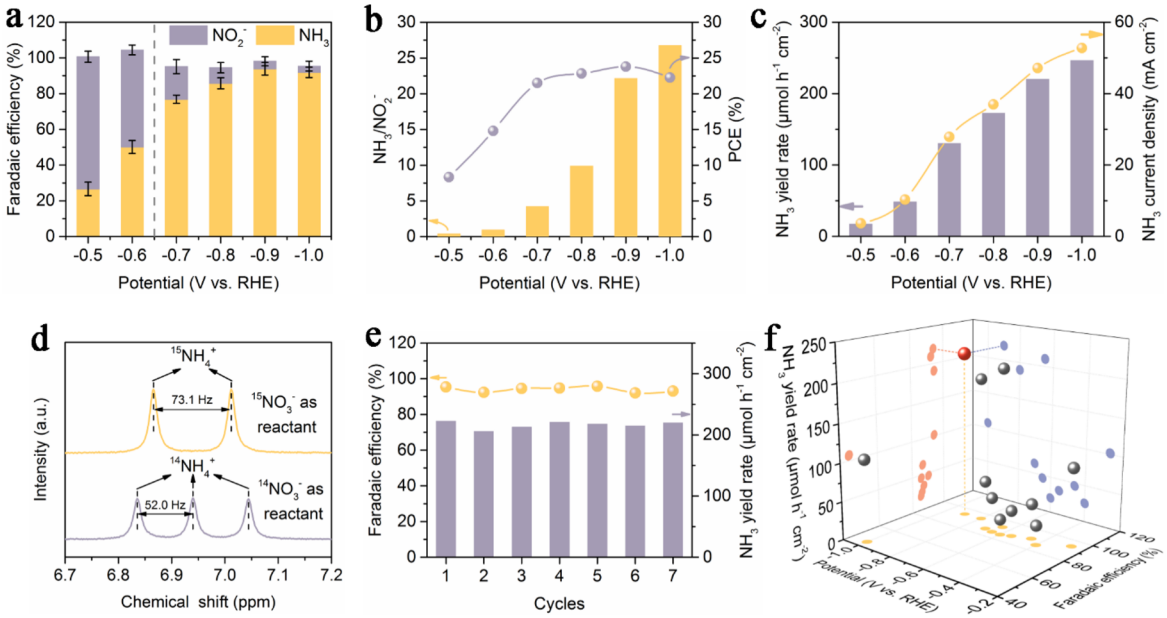

Figure 2. Electrocatalytic NO_3RR performance of c-Cu/Cu_2O in 0.1 M PB solution containing 0.1 M KNO_3. (a) Faradaic efficiencies of NH_3 and NO_2^- at different potentials. (b) Faradaic efficiency ratio of NH_3 to NO_2^- and cathode power conversion efficiency (PCE) at different potentials. (c) The corresponding NH_3 production rate and partial current density at different potentials. (d) ^1H NMR spectra of $^{14}NH_4^+$ and $^{15}NH_4^+$ produced after NO_3RR using $^{15}NO_3^-$ and $^{14}NO_3^-$ as reactants, respectively. (e) Cycling stability measurements of c-Cu/Cu_2O at −0.9 V vs RHE. (f) Performance comparison of different reported Cu-based catalysts for NO_3^- electroreduction to NH_3 in neutral electrolyte (See detailed information in Table S1). Red ball represents the performance of this work. The error bars represent the standard deviation of three independent samples.

fabricated via an electrochemical prereduction method, and the structural evolution of Cu-based catalysts during the NO_3RR at different potentials was systematically investigated. The effect of the chemical state of Cu on the product selectivity of the NO_3RR was verified utilizing a rational electrochemical strategy combined with in situ Raman spectroscopy and theoretical calculations. Results show that the Cu/Cu_2O interface formed at low reduction potentials (≥−0.6 V vs reversible hydrogen electrode (RHE)) facilitates the conversion of NO_3^- to NO_2^-. By contrast, at high reduction potentials (<−0.6 V vs RHE), the in situ generated oxide-derived Cu^0 (OD-Cu) is the genuine active phase for the highly selective NO_3^- reduction to NH_3. The OD-Cu cube exhibits a maximum NH_3 Faradaic efficiency (FE) of 93.9% and a productivity of 219.8 μmol h^{-1} cm^{-2} at −0.9 V vs RHE. ^{15}N isotope-labeling experiments confirm that the detected NH_3 originates from the NO_3RR. In situ infrared (IR) spectroscopy analysis and density functional theory (DFT) calculations show that the improved NH_3 selectivity on OD-Cu is because of the enhanced adsorption of NO_3^-, the promoted formation of key intermediate *NOH, and the inhibited competitive HER. Our results provide a comprehensive fundamental understanding on the nature of the active sites for the selective NO_3RR on Cu-based electrocatalysts and will guide the rational optimization of efficient electrocatalysts for NH_3 production.

2. RESULTS AND DISCUSSION

Cu_2O cubes, referred to as c-Cu_2O, were synthesized by a modified method,[42] as proven using scanning electron microscopy (SEM), transmission electron microscopy (TEM), X-ray diffraction (XRD), X-ray photoelectron spectroscopy (XPS), and Raman results (Figures S1−S5). Notably, a neutral phosphate buffer (PB) solution was used as the electrolyte in the electrochemical reduction method because it could inhibit the competitive HER.[43,44] Therefore, first, the c-Cu_2O precursors were drop-coated on carbon paper; then, electrochemical prereduction reconstruction was performed at a bias potential of −0.6 V vs RHE in a 0.1 M PB solution (pH = 7) until a stable current was achieved (Figures 1a and S6). XRD results of the c-Cu_2O precursors display two characteristic peaks at 36.5° and 42.4°, attributed to the (111) and (200) facets of Cu_2O (JCPDS 77-0199; Figure 1b), respectively. These characteristic peaks of Cu_2O are still observed in the XRD spectra after prereduction stabilization along with a new set of peaks corresponding to metallic Cu (JCPDS 04-0836), suggesting the presence of a relatively stable bulk structure of the synthesized Cu_2O precursor with only partial reduction of Cu_2O to metallic Cu. SEM images clearly show that the Cu-based catalysts inherit the original bulk structure of the Cu_2O precursors but exhibit an increased surface roughness after prereduction (Figure S7), improving the electrochemically active surface area (ECSA) and exposing more reaction sites (Figure S8).

In situ Raman spectroscopy was further performed in a commercial H-type Raman cell to monitor the dynamic phase evolution during the prereduction of Cu_2O (Figures 1c and S9). The characteristic Raman modes of Cu_2O (221, 419, 524, and 630 cm^{-1}) are preserved but exhibit a weakened intensity after the prereduction process, implying that the Cu_2O precursor is not completely reduced. The coexistence of Cu and Cu_2O structures was obtained using this prereduction approach. To further illustrate the structure and composition of Cu_2O after prereduction, high-resolution transmission electron microscopy (HRTEM) of the edge region for c-Cu_2O was performed immediately after prereduction (Figure 1d). Only surficial Cu_2O was reduced to Cu particles

https://doi.org/10.1021/acscatal.3c01315
ACS Catal. 2023, 13, 7529−7537

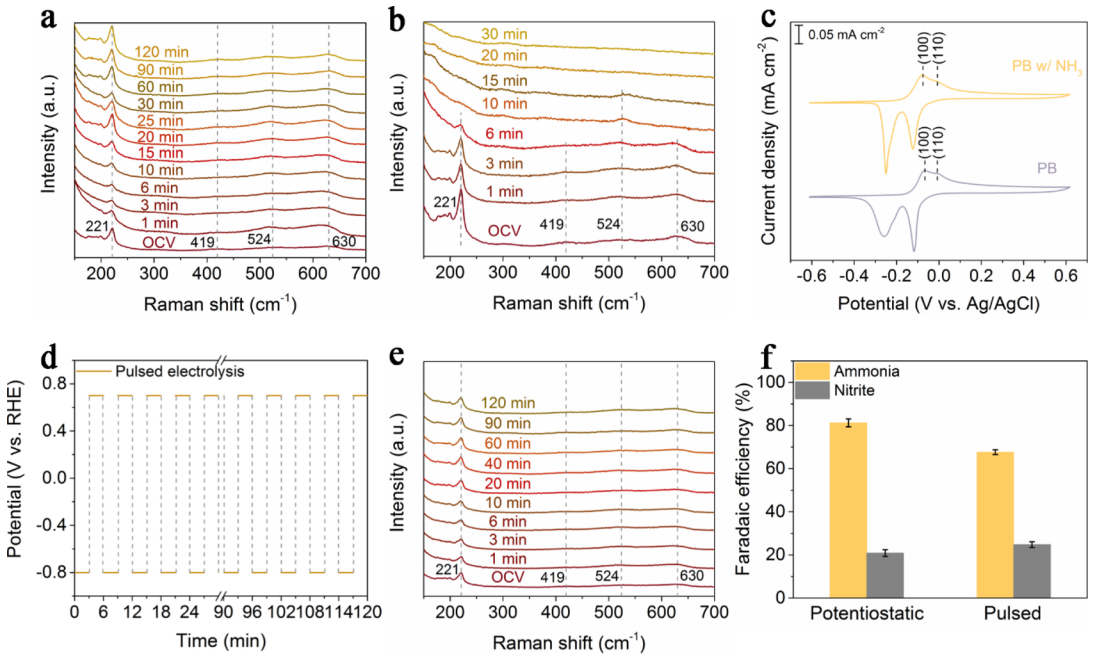

Figure 3. Pulsed electrolysis measurements. In situ Raman spectra of c-Cu/Cu_2O as a function of reaction time at (a) − 0.6 and (b) − 0.9 V vs RHE, respectively. (c) CV curves of OD-Cu-c in 0.1 M PB electrolyte with and without 0.01 M ammonia. The scan rate is 1 mV s^{-1}. (d) Periodic reduction and oxidation of c-Cu/Cu_2O under NO_3^- pulsed electrolysis at E_{ca} = −0.8 V and E_{an} = 0.7 V vs RHE. (e) In situ Raman spectra of c-Cu/Cu_2O as a function of reaction time under pulsed electrolysis. (f) Comparison of Faradaic efficiencies of NH_3 and NO_2^- for c-Cu/Cu_2O under different electrolysis conditions.

belonging to the (200) planes, while the bulk phase was relatively stable, as indicated by the observed single-crystal nature in the fast Fourier transform (FFT) pattern (inset in Figure 1d). Scanning transmission electron microscopy-energy dispersive X-ray spectroscopy (STEM-EDS, Figure 1e and Figure S10) images show that the surface and bulk of c-Cu_2O have different Cu and O atomic contents after prereduction, unlike the initial c-Cu_2O, which has a uniform distribution of Cu and O elements (Figure S11). The atomic contents of the bulk phase are similar to those of c-Cu_2O before prereduction, and only Cu atoms are detected on the surface, further confirming the uniform spatial distribution of metallic Cu nanoparticles on the surface. Therefore, a Cu/Cu_2O interface structure is successfully formed from c-Cu_2O via the prereduction method, which is used as a model electrocatalyst for the subsequent NO_3RR. For convenience, the Cu/Cu_2O interface structure is hereafter denoted as c-Cu/Cu_2O.

The NO_3^- electroreduction performance of c-Cu/Cu_2O was assessed under ambient conditions in a standard three-electrode H-type electrolytic cell. Chronoamperometry tests were performed in a 0.1 M PB electrolyte containing 0.1 M KNO_3 over a potential ranging from −0.5 to −1.0 V vs RHE for 2 h. Indophenol blue spectrophotometry and ^{1}H NMR spectroscopy were used to determine the concentration of NH_3, and the possible byproduct NO_2^- was quantified via ion chromatography (Figures S12−S14). To assess the selectivity of specific products, the potential-dependent FEs of NH_3 and NO_2^- are shown in Figure 2a. When the applied potential is more positive than −0.6 V vs RHE, the predominant reduction product is NO_2^-, whereas NH_3 is the main product when the applied potential is more negative than −0.6 V vs RHE. Specifically, at −0.9 V vs RHE, c-Cu/Cu_2O exhibits a maximum NH_3 FE of 93.9%. Notably, the sum of the FEs for reduction products NH_3 and NO_2^- is approximately 100% over the entire applied potential range, suggesting that the NO_3RR can effectively inhibit the HER. Additionally, the NH_3 and NO_2^- ratios of the c-Cu/Cu_2O catalyst were compared (Figure 2b). At −0.9 V vs RHE, the c-Cu/Cu_2O catalyst exhibits the highest NH_3 to NO_2^- ratio of 22.1, further indicating that c-Cu/Cu_2O preferentially produces NH_3 rather than NO_2^- at high cathodic potentials. Furthermore, the half-cell power conversion efficiency (PCE) of c-Cu/Cu_2O for NH_3 is 23.8% at −0.9 V vs RHE. The yield rate (Y_{NH3}) and partial current density (J_{NH3}) of NH_3 increase with an increase in cathodic potential (Figure 2c), consistent with previous reports.[28,45] Impressively, c-Cu/Cu_2O exhibits an NH_3 yield rate and partial current density of up to 246.2 μmol h^{-1} cm^{-2} and 52.8 mA cm^{-2} at −1.0 V vs RHE, respectively.

To verify that the generated NH_3 was from the NO_3RR instead of other nitrogenous pollutants, $K^{15}NO_3$ was used as the starting nitrogen source in the ^{15}N isotope-labeling experiments. As shown in the ^{1}H NMR spectra (Figure 2d), when $^{14}NO_3^-$ is used as the reactant for the electrolysis reaction, the ^{1}H NMR spectrum of the detected NH_4^+ exhibits a typical three-peak feature with a coupling constant of 52.0 Hz, whereas when $^{14}NO_3^-$ is replaced by $^{15}NO_3^-$, the ^{1}H NMR spectrum of the detected $^{15}NH_4^+$ exhibits a typical double-peak feature with a coupling constant of 73.1 Hz. The ^{15}N isotope-labeling results strongly suggested that NH_3 detected in the electrolyte is indeed from the NO_3RR.[46] As determined using ^{1}H NMR spectroscopy, the corresponding FE and yield rate of c-Cu/Cu_2O for NH_3 production at −0.9 V vs RHE are 93.6% and 217.7 μmol h^{-1} cm^{-2}, respectively, consistent with the UV−Vis spectra (Figure S15). No NH_3 is detected when blank PB solutions are used for electrolysis, confirming that NH_3 is produced only via the electroreduction of NO_3^-. The durability of the c-Cu/Cu_2O catalyst was verified by performing continuous NO_3^- electrolysis at −0.9 V

https://doi.org/10.1021/acscatal.3c01315
ACS Catal. 2023, 13, 7529−7537

vs RHE. As shown in Figure 2e, the NH_3 yield rate and FE remain stable over the seven consecutive rounds of the reaction, without an apparent trend of decay. When the electrolytes after electrolysis are stained with an indophenol blue indicator, they all show an almost identical color, again demonstrating the good catalytic stability of the Cu-based material (Figure S16).

The structure of the c-Cu/Cu_2O catalyst after NO_3^- reduction electrolysis at different potentials was characterized via ex situ XRD (Figure S17). The c-Cu/Cu_2O catalyst undergoes a phase transition as the cathodic potential increases from −0.5 to −1.0 V vs RHE. Specifically, the initial Cu/Cu_2O interface structure is reconstructed into the metallic state Cu when the reaction potential is more negative than −0.6 V vs RHE. However, the original cubic morphology of the c-Cu/Cu_2O catalyst is still preserved at operation potentials of −0.6 and −0.9 V vs RHE (Figure S18). The morphology and phase analyses of c-Cu/Cu_2O after the durability test at −0.9 V vs RHE further reveal that the initial Cu/Cu_2O mixed phase is reconstructed into the metallic state Cu^0 without morphological damage (Figures S19 and S20). Therefore, the in situ generated OD-Cu is the true active phase during the first electrolysis and shows excellent stability for the subsequent selective NO_3^- electroreduction to NH_3. Additionally, the NO_3RR performance of the oxide-derived Cu cube (abbreviated as OD-Cu-c) was compared with those of other recently reported Cu-based catalysts. Figure 2f and Table S1 show that OD-Cu-c has a superior NH_3 yield rate and FE for the electroreduction of NO_3^- to NH_3 in a neutral electrolyte than most other Cu-based materials.

To further investigate the effect of different oxidation states of copper on the NH_3 selectivity during NO_3^- reduction, the structural evolution of the c-Cu/Cu_2O catalysts under different applied potentials was monitored via in situ Raman spectroscopy. As depicted in Figure 3a, c-Cu/Cu_2O retains the characteristic Raman modes of Cu_2O (e.g., the $2\Gamma^-_{12}$ mode at 221 cm^{-1}) throughout the 2 h reaction when the applied potential is −0.6 V vs RHE.[47] However, when a negative potential of −0.9 V vs RHE is applied, the intensity of the Cu_2O peak gradually decreases and disappears within 15 min, indicating the complete reduction of the oxide to the metallic phase (Figure 3b). The results are consistent with the ex situ XRD characterization and further indicate that the oxide-derived metallic phase Cu^0 is the true active phase for promoting the highly selective NH_3 synthesis from NO_3^- at −0.9 V vs RHE. To further confirm the universality of this conclusion, Cu_2O octahedron precursors (abbreviated as o-Cu_2O) were also synthesized, and the true active centers and their role in determining the selectivity of the NO_3^- reduction product were investigated using the same strategy (Figures S1−S7, S11, S17, S18, and S21−S24). The results showed that the potential-induced OD-Cu from the o-Cu_2O precursor is also the active phase for NH_3 production.

Additionally, linear sweep voltammetry (LSV) tests for NO_3^- reduction were performed on the OD-Cu-c catalyst in a 0.1 M PB solution with and without 0.1 M KNO_3 (Figure S25). Compared with the blank electrolyte, the increase in current density and positive shift of the onset potential of OD-Cu-c in PB solution containing 0.1 M KNO_3 indicate the catalytic activity for the NO_3RR. And the reduction peak at −0.4 V vs RHE is attributed to NH_3 generation.[48] Moreover, the LSV curves of OD-Cu-c highly overlap for five consecutive cycles, further verifying the excellent stability of the OD-Cu-c catalyst. The advantages of the OD-Cu-c catalyst are further highlighted by performance comparison with commercial Cu microspheres (referred to as Cu MSs) with a similar particle size (Figure S26). The ECSA of different Cu-based samples was estimated using cyclic voltammetry (CV) measurements under a potential window without Faraday reactions at different scan rates (Figure S27). LSV curves showed that OD-Cu-c exhibits a larger current density than Cu MSs under the same test conditions (Figure S28). Moreover, the higher intrinsic NO_3RR activity of OD-Cu-c than Cu MSs can be further gleaned from the larger current density in the ECSA-normalized LSV curves. Potentiostatic electrocatalysis results show that the selectivity of NH_3 over OD-Cu-c is higher than that over Cu MSs in the potential ranging from −0.7 to −1.0 V vs RHE. For example, at −0.9 V vs RHE, OD-Cu-c and Cu MSs exhibit FEs of 93.88 and 81.69%, respectively. Furthermore, the turnover frequency (TOF) was calculated to evaluate the ability of the catalyst to convert the reactants into the desired products per catalytic site and per unit of time.[49] The TOFs of OD-Cu-c and Cu MSs for NH_3 production are 1.09×10^{-2} and 4.73×10^{-3} s^{-1} at −0.9 V vs RHE, respectively. These results suggest that the in situ formed Cu^0 catalyst during the electrolysis process enables an efficient NO_3RR to NH_3.[41] The apparent activation energy (E_a) of different Cu-based samples for NO_3^- reduction to NH_3 was evaluated using their temperature-dependent performances and Arrhenius equation.[49] Figure S29 shows that the apparent activation energy of OD-Cu-c (E_a = 11.3 kJ mol^{-1}) is lower than that of Cu/Cu_2O (E_a = 12.3 kJ mol^{-1}) at a potential of −0.6 V vs RHE. At a potential of −0.9 V vs RHE, the E_a of OD-Cu-c is only 5.3 kJ mol^{-1}, which is one-third of that of Cu MSs (E_a = 16.1 kJ mol^{-1}). OD-Cu-c has a lower energy barrier than Cu/Cu_2O and Cu MSs for initiating electrocatalytic NO_3^- to NH_3 and thus exhibits a high intrinsic activity. The microstructures of OD-Cu-c and Cu MSs were characterized by HRTEM (Figure S30a−c). The results indicated that OD-Cu-c displays a Cu(100)-rich surface compared to Cu MSs dominated by Cu(111) facets, which was further confirmed by specific electrochemical adsorption voltammetry tests of OH^- on different facets of Cu (Figure S30d).[26,50] Therefore, compared with Cu MSs, the high (100) surface fraction of OD-Cu-c might be responsible for its high intrinsic activity.

To study the effect of the oxidation state of Cu on the selectivity of NO_3^- reduction products, pulsed electrolysis[51−53] was well-designed to modulate the chemical state composition of the c-Cu/Cu_2O catalyst through the periodic application of oxidative potential pulses over a short period. Before that, the electrochemical behavior of NH_3 oxidation over OD-Cu-c was first investigated (Figure 3c). Similar to the blank 0.1 M PB electrolyte, when the electrolyte comprises 0.1 M PB and 0.01 M NH_3 by the addition of concentrated NH_3 water (corresponding to the amount of NH_3 produced via NO_3RR), only two peaks ascribed to OH^- adsorption on the Cu(100) and Cu(110) surfaces are observed throughout the potential interval.[26] The absence of new oxidation peaks indicates that the Cu-based catalyst is inactive for electrocatalytic NH_3 oxidation. Therefore, pulsed electrolysis experiments were performed by periodically applying a reduction potential of −0.8 V vs RHE and an oxidation potential of 0.7 V vs RHE, respectively (Figure 3d). For comparison, potentiostatic electrolysis experiments of the NO_3RR at −0.8 V vs RHE were also performed (Figure S31). The structural evolution of the c-Cu/Cu_2O catalyst during pulsed electrolysis was

https://doi.org/10.1021/acscatal.3c01315
ACS Catal. 2023, 13, 7529−7537

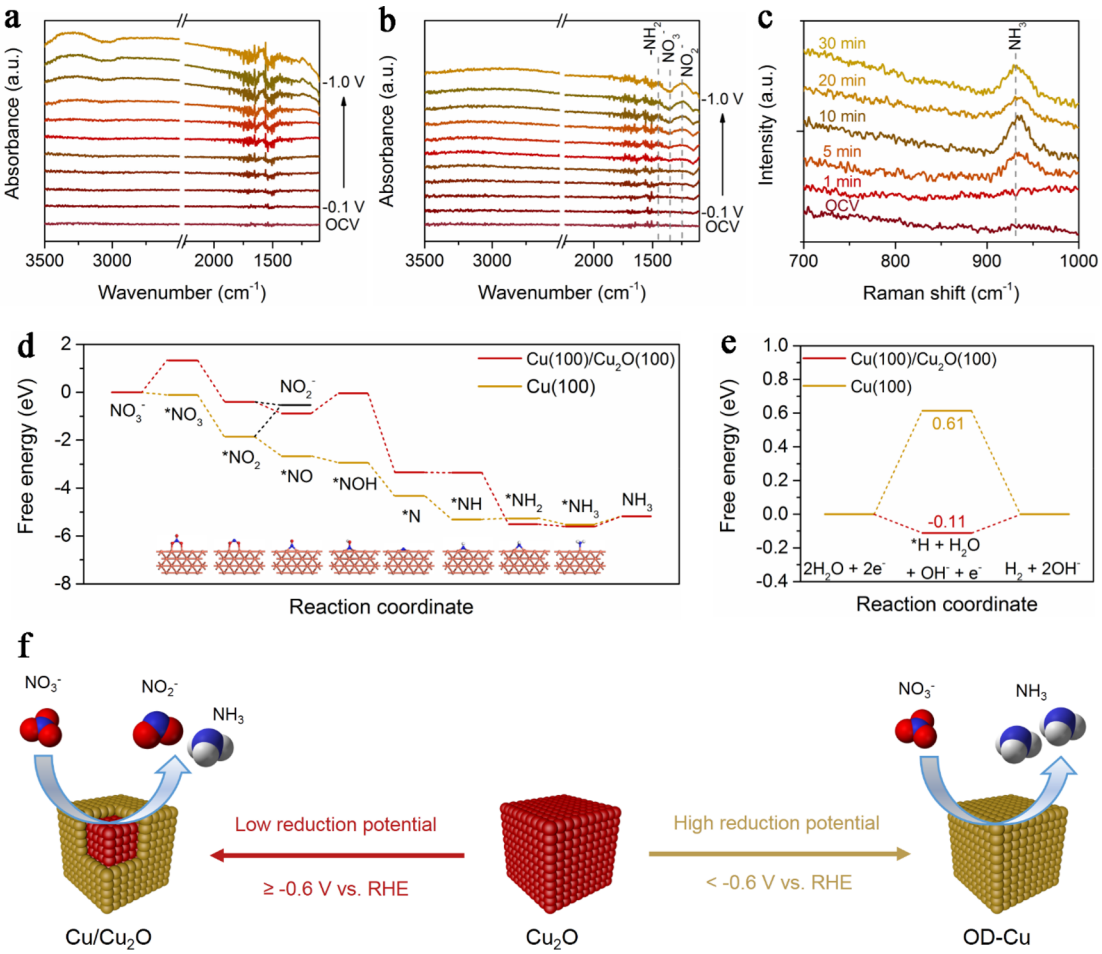

Figure 4. In situ spectroscopic characterization and theoretical calculations. (a) In situ ATR-FTIR spectra of OD-Cu-c acquired in 0.1 M PB solution. (b) In situ ATR-FTIR spectra of OD-Cu-c in 0.1 M PB solution containing 0.1 M KNO_3. (c) In situ Raman spectra of OD-Cu-c obtained under NO_3RR at −0.9 V vs RHE. (d) The calculated free energy of NO_3RR to NH_3 and NO_2^- on Cu(100) and Cu/Cu_2O at 0 V vs RHE (T = 298.15 K). The coverage of species on both Cu(100) and $Cu(100)/Cu_2O(100)$ surfaces is 25%. The red, gray, blue, and orange balls represent oxygen, hydrogen, nitrogen, and copper atoms, respectively. (e) The reaction energies for the formation of H_2 on Cu(100) and Cu/Cu_2O. (f) Schematic illustration of potential-induced electrochemical reconstruction of Cu_2O cubes with different chemical states of Cu toward NO_3^- reduction to different products (NH_3 and NO_2^-).

monitored via in situ Raman spectroscopy (Figure 3e). During the pulsed electrolysis process, the Raman characteristic peaks attributed to Cu_2O are always present in the Raman spectra, suggesting that pulsed electrolysis can protect the Cu^+ species of the c-Cu/Cu_2O catalyst during the reduction reaction. Ex situ XRD results further show the presence of a mixed oxidation state of Cu^0 and Cu^+ in the c-Cu/Cu_2O catalyst after pulsed electrolysis (Figure S32). By quantifying NH_3 and NO_2^- produced under different reaction conditions, it was found that the pulsed electrolysis decreases (13.6%) the NH_3 selectivity, compared to that obtained via potentiostatic electrolysis on c-Cu/Cu_2O, along with increased selectivity (3.9%) of NO_2^- (Figure 3f). Additionally, the NH_3 to NO_2^- ratio of c-Cu/Cu_2O during potentiostatic electrolysis is 3.9, which is better than that during pulsed electrolysis (2.7; Figure S33). Consequently, the NH_3 yield rate is higher during potentiostatic than pulsed electrolysis, where the total charge across the electrodes is similar and the NO_3^- conversion is comparable (Figure S34). SEM images of the catalysts after pulsed electrolysis show that this selectivity difference is irrelevant to the morphological reconstruction (Figure S35). Therefore, the Cu/Cu_2O interface structure primarily facilitates the conversion of NO_3^- to NO_2^-, while the in situ reconstructed Cu^0 species favor the continuous protonation of NO_3^- for NH_3 synthesis.

In situ spectroscopic measurement and theoretical calculations were performed to understand the reaction mechanism of NO_3^- reduction at the molecular level. In situ attenuated total reflectance Fourier transform infrared (ATR-FTIR) spectroscopy was performed for the NO_3RR process over OD-Cu-c in the applied potential ranging from −0.1 to −1.0 V vs RHE. In the NO_3^--free PB electrolyte (Figure 4a), the FTIR spectra show only two positive peaks at 3311 and 1595 cm^{-1}, corresponding to O−H stretching and H−O−H bending of water molecules, respectively.[54] The increase in the intensity of these peaks as the potential becomes more negative indicates the occurrence of the HER with strong adsorption of water molecules. The characteristic IR bands during the NO_3RR were observed as early as −0.5 V vs RHE (Figure 4b). Specifically, the intensity of the negative peak at ∼1350 cm^{-1} in the FTIR spectrum, attributed to the adsorption of NO_3^-,[55] increases negatively with an increase in cathodic potential because of the continuous consumption of NO_3^- on the OD-Cu-c catalyst surface. Meanwhile, the concomitant peak at

https://doi.org/10.1021/acscatal.3c01315
ACS Catal. 2023, 13, 7529−7537

1250 cm^{-1} in the FTIR spectrum is ascribed to the stretching mode of NO_2^-, suggesting that NO_2^- is an intermediate product during the reduction process.[56] Furthermore, the characteristic peak of the bending vibration of the $-NH_2$ intermediate at 1450 cm^{-1} in the FTIR spectrum reflects NH_3 production from NO_3^- after successive hydrodeoxygenation.[39] Notably, compared to the results obtained in the blank electrolyte, the IR vibrational signals of OD-Cu-c assigned to the adsorbed water molecules are very weak over the entire range of applied potential in the NO_3^--containing solution, probably because of the adsorption of NO_3^- on the catalytic sites and suppression of the HER by the NO_3RR. Additionally, similar fingerprints of nitrogen-containing intermediates, including NO_3^-, NO_2^-, and $-NH_2$ species, were observed in the FTIR spectrum of OD-Cu octahedrons, indicating that OD-Cu octahedrons share the same NO_3^- reduction reaction pathway as OD-Cu-c (Figure S36). In situ Raman spectra obtained at an operating potential of −0.9 V vs RHE are shown in Figures 4c and S37. The typical Raman peak of NH_3 at ∼936 cm^{-1} gradually appears at the fifth minute on the surface of OD-Cu-c, further confirming that NH_3 is produced via the NO_3RR.[57]

Based on the intermediates detected using the above spectroscopy and previous reports,[58] the reaction pathway for the synthesis of NH_3 via NO_3^- reduction on Cu and Cu/Cu_2O can be deduced. The Gibbs free energy of the reaction pathway (*NO_3 → *NO_2 → *NO → *N → *NH → *NH_2 → *NH_3) was further calculated using DFT. The adsorption configurations of the intermediates of the NO_3RR to NH_3 on the Cu(100) and Cu/Cu_2O surfaces are shown in Figures S38−S40, respectively. The adsorption of reactants on the catalyst surface is generally a prerequisite for the reaction.[45] As shown in the Gibbs free energy diagram in Figure 4d, the adsorption of NO_3^- on Cu(100) (−0.11 eV) is spontaneous, whereas the adsorption of NO_3^- on Cu/Cu_2O (1.33 eV) is endothermic, indicating the enhanced NO_3^- adsorption of Cu(100). On Cu/Cu_2O, the hydrogenation of *NO species (*NO → *NOH) requires an energy of up to 0.84 eV, and therefore, this is the potential-determining step (PDS). Remarkably, the PDS of Cu(100) is the desorption of *NH_3 with an energy barrier of 0.34 eV, which is lower than that of Cu/Cu_2O. Therefore, a considerably lower reaction barrier for the generation of NH_3 via the NO_3RR is obtained on Cu(100). Furthermore, the generation of NO_2^- on Cu(100) requires an energy of up to 1.34 eV, which is larger than the reaction barrier of the PDS for NH_3, confirming that NH_3 formation is more favorable on Cu^0 active sites. By contrast, after NO_3^- adsorption, the reaction process from NO_3^- to NO_2^- on the Cu/Cu_2O surface is thermodynamically downhill, indicating the preferential production of NO_2^-. Additionally, the ΔG for H_2 formation on the Cu(100) surface is higher than that on Cu/Cu_2O, indicating the inhibition of the HER on the Cu(100) surface (Figure 4e).[39] The adsorption energy of NO_3^- (ΔG_{*NO3}) on Cu(100) and Cu(111) was also calculated (Figure S41). The results show the strong adsorption of NO_3^- on Cu(100) than Cu(111); therefore, Cu(100) exhibits more favorable NO_3RR performance than Cu(111), in agreement with the literature.[59,60] The enhanced adsorption of NO_3^- on Cu(100) originates from its electronic structure with the d-band center closer to the Fermi level, as illustrated by the projected density of states analysis.[14,20] These results indicate that OD-Cu and Cu/Cu_2O synthesized via the potential-induced method exhibited different product selectivities for NO_3^- reduction, respectively (Figure 4f). OD-Cu is the genuine active phase that promotes the highly selective synthesis of NH_3 from NO_3^-. By contrast, the presence of Cu^+ favors the production of NO_2^-. Additionally, the catalytic activity of metallic Cu is related to the crystal plane due to the different electronic structures.

3. CONCLUSIONS

In summary, a Cu/Cu_2O interface model catalyst was developed for highly selective NO_3^- reduction to NH_3, and the nature of Cu active sites and their correlation with the catalytic performance during the working process were studied. Importantly, in situ Raman spectroscopy and ex situ XRD characterizations show that Cu_2O of Cu/Cu_2O undergoes a structural transformation to the oxide-derived Cu^0 when the applied potential changes from −0.5 to −1.0 V vs RHE. The oxide-derived Cu cube catalyst exhibits a maximum NH_3 FE of 93.9% and a productivity of 219.8 μmol h^{-1} cm^{-2} at −0.9 V vs RHE. The well-designed pulse electrolysis experiments, in situ IR/Raman, and theoretical calculation analysis show that the reconstituted Cu^0 is favorable for the highly selective NH_3 generation, whereas the Cu/Cu_2O interface prefers NO_2^- formation. This study provides an insight into the selective NO_3RR over Cu-based catalysts and valuable guidance for the rational optimization of efficient electrocatalysts.

■ ASSOCIATED CONTENT

Supporting Information

The Supporting Information is available free of charge at https://pubs.acs.org/doi/10.1021/acscatal.3c01315.

Materials and methods; characterization data such as SEM images, TEM images, XRD patterns, XPS spectra, in situ Raman spectra, HAADF-STEM image, EDS patterns, UV−Vis absorption spectra, ion chromatogram spectra, ^{1}H NMR spectra, in situ ATR-FTIR spectra; electrochemical measurements; computational details and modeling (PDF)

■ AUTHOR INFORMATION

Corresponding Authors

Xinbo Zhang − *State Key Laboratory of Rare Earth Resource Utilization, Changchun Institute of Applied Chemistry, Chinese Academy of Sciences, Changchun 130022, P. R. China; School of Applied Chemistry and Engineering, University of Science and Technology of China, Hefei 230026, P. R. China;* orcid.org/0000-0002-5806-159X; Email: xbzhang@ciac.ac.cn

Haixia Zhong − *State Key Laboratory of Rare Earth Resource Utilization, Changchun Institute of Applied Chemistry, Chinese Academy of Sciences, Changchun 130022, P. R. China; School of Applied Chemistry and Engineering, University of Science and Technology of China, Hefei 230026, P. R. China;* orcid.org/0000-0002-2839-0253; Email: hxzhong@ciac.ac.cn

Di Bao − *State Key Laboratory of Rare Earth Resource Utilization, Changchun Institute of Applied Chemistry, Chinese Academy of Sciences, Changchun 130022, P. R. China*; Email: dbao@ciac.ac.cn

Authors

Na Zhou − *State Key Laboratory of Rare Earth Resource Utilization, Changchun Institute of Applied Chemistry,*

https://doi.org/10.1021/acscatal.3c01315
ACS Catal. 2023, 13, 7529−7537

Chinese Academy of Sciences, Changchun 130022, P. R. China; School of Applied Chemistry and Engineering, University of Science and Technology of China, Hefei 230026, P. R. China

Zhi Wang − *State Key Laboratory of Rare Earth Resource Utilization, Changchun Institute of Applied Chemistry, Chinese Academy of Sciences, Changchun 130022, P. R. China; School of Applied Chemistry and Engineering, University of Science and Technology of China, Hefei 230026, P. R. China*

Ning Zhang − *State Key Laboratory of Rare Earth Resource Utilization, Changchun Institute of Applied Chemistry, Chinese Academy of Sciences, Changchun 130022, P. R. China; School of Applied Chemistry and Engineering, University of Science and Technology of China, Hefei 230026, P. R. China*

Complete contact information is available at: https://pubs.acs.org/10.1021/acscatal.3c01315

Author Contributions

All authors have given approval to the final version of the manuscript.

Notes

The authors declare no competing financial interest.

■ ACKNOWLEDGMENTS

This work was supported by National Key R&D Program of China (2021YFB4000402), the National Natural Science Foundation of China (52071311, 52273277, 52072362, and 21905269), Jilin Province Science and Technology Development Plan Funding Project (20200201079JC and 20220201112GX), and Youth Innovation Promotion Association CAS (2021223). H.X.Z. acknowledges funding from National Natural Science Foundation of China Outstanding Youth Science Foundation of China (Overseas).

■ REFERENCES

(1) Erisman, J. W.; Sutton, M. A.; Galloway, J.; Klimont, Z.; Winiwarter, W. How a Century of Ammonia Synthesis Changed the World. *Nat. Geosci.* **2008**, *1*, 636−639.

(2) Kitano, M.; Inoue, Y.; Yamazaki, Y.; Hayashi, F.; Kanbara, S.; Matsuishi, S.; Yokoyama, T.; Kim, S.-W.; Hara, M.; Hosono, H. Ammonia Synthesis Using a Stable Electride as an Electron Donor and Reversible Hydrogen Store. *Nat. Chem.* **2012**, *4*, 934−940.

(3) Christensen, C. H.; Johannessen, T.; Sørensen, R. Z.; Nørskov, J. K. Towards an Ammonia-Mediated Hydrogen Economy? *Catal. Today* **2006**, *111*, 140−144.

(4) Li, J.; Xiao, Y.; Shui, F.; Yi, M.; Zhang, Z.; Liu, X.; Zhang, L.; You, Z.; Yang, R.; Yang, S.; et al. Extremely Stable Sulfuric Acid Covalent Organic Framework for Highly Effective Ammonia Capture. *Chin. J. Chem.* **2022**, *40*, 2445−2450.

(5) Xu, J.; Yan, H.; Jin, Z.; Jia, C.-J. Facile Synthesis of Stable MO_2N Nanobelts with High Catalytic Activity for Ammonia Decomposition. *Chin. J. Chem.* **2019**, *37*, 364−372.

(6) Chen, F.-Y.; Wu, Z.-Y.; Gupta, S.; Rivera, D. J.; Lambeets, S. V.; Pecaut, S.; Kim, J. Y. T.; Zhu, P.; Finfrock, Y. Z.; Meira, D. M.; et al. Efficient Conversion of Low-concentration Nitrate Sources into Ammonia on a Ru-Dispersed Cu Nanowire Electrocatalyst. *Nat. Nanotechnol.* **2022**, *17*, 759−767.

(7) Bao, D.; Zhang, Q.; Meng, F.-L.; Zhong, H.-X.; Shi, M.-M.; Zhang, Y.; Yan, J.-M.; Jiang, Q.; Zhang, X.-B. Electrochemical Reduction of N_2 under Ambient Conditions for Artificial N_2 Fixation and Renewable Energy Storage Using N_2/NH_3 Cycle. *Adv. Mater.* **2017**, *29*, 1604799.

(8) Soloveichik, G. Electrochemical Synthesis of Ammonia as a Potential Alternative to the Haber−Bosch Process. *Nat. Catal.* **2019**, *2*, 377−380.

(9) Cui, X.; Tang, C.; Zhang, Q. A Review of Electrocatalytic Reduction of Dinitrogen to Ammonia under Ambient Conditions. *Adv. Energy Mater.* **2018**, *8*, 1800369.

(10) Wang, Y.; Shi, M.-M; Bao, D.; Meng, F.-L.; Zhang, Q.; Zhou, Y.-T.; Liu, K.-H.; Zhang, Y.; Wang, J.-Z.; Chen, Z.-W.; et al. Generating Defect-Rich Bismuth for Enhancing the Rate of Nitrogen Electroreduction to Ammonia. *Angew. Chem., Int. Ed.* **2019**, *58*, 9464−9469.

(11) Luo, Y.; Liang, S.; Wang, X.; Lin, B.; Chen, C.; Jiang, L. Facile Synthesis and High-Value Utilization of Ammonia. *Chin. J. Chem.* **2022**, *40*, 953−964.

(12) Shi, M.-M.; Bao, D.; Wulan, B.-R.; Li, Y.-H.; Zhang, Y.-F.; Yan, J.-M.; Jiang, Q. Au Sub-Nanoclusters on TiO_2 toward Highly Efficient and Selective Electrocatalyst for N_2 Conversion to NH_3 at Ambient Conditions. *Adv. Mater.* **2017**, *29*, 1606550.

(13) Tang, C.; Qiao, S.-Z. How to Explore Ambient Electrocatalytic Nitrogen Reduction Reliably and Insightfully. *Chem. Soc. Rev.* **2019**, *48*, 3166−3180.

(14) Wang, Y.; Li, H.; Zhou, W.; Zhang, X.; Zhang, B.; Yu, Y. Structurally Disordered RuO_2 Nanosheets with Rich Oxygen Vacancies for Enhanced Nitrate Electroreduction to Ammonia. *Angew. Chem., Int. Ed.* **2022**, *61*, No. e202202604.

(15) Lv, C.; Zhong, L.; Liu, H.; Fang, Z.; Yan, C.; Chen, M.; Kong, Y.; Lee, C.; Liu, D.; Li, S.; et al. Selective Electrocatalytic Synthesis of Urea with Nitrate and Carbon Dioxide. *Nat. Sustain.* **2021**, *4*, 868−876.

(16) Duca, M.; Koper, M. T. M. Powering Denitrification: the Perspectives of Electrocatalytic Nitrate Reduction. *Energy Environ. Sci.* **2012**, *5*, 9726−9742.

(17) Wang, Y.; Wang, C.; Li, M.; Yu, Y.; Zhang, B. Nitrate Electroreduction: Mechanism Insight, In situ Characterization, Performance Evaluation, and Challenges. *Chem. Soc. Rev.* **2021**, *50*, 6720−6733.

(18) van Langevelde, P. H.; Katsounaros, I.; Koper, M. T. M. Electrocatalytic Nitrate Reduction for Sustainable Ammonia Production. *Joule* **2021**, *5*, 290−294.

(19) Wang, C.; Ye, F.; Shen, J.; Xue, K.-H.; Zhu, Y.; Li, C. In Situ Loading of Cu_2O Active Sites on Island-like Copper for Efficient Electrochemical Reduction of Nitrate to Ammonia. *ACS Appl. Mater. Interfaces* **2022**, *14*, 6680−6688.

(20) Liu, H.; Park, J.; Chen, Y.; Qiu, Y.; Cheng, Y.; Srivastava, K.; Gu, S.; Shanks, B. H.; Roling, L. T.; Li, W. Electrocatalytic Nitrate Reduction on Oxide-Derived Silver with Tunable Selectivity to Nitrite and Ammonia. *ACS Catal.* **2021**, *11*, 8431−8442.

(21) Zhang, H.; Wang, C.; Luo, H.; Chen, J.; Kuang, M.; Yang, J. Iron Nanoparticles Protected by Chainmail-structured Graphene for Durable Electrocatalytic Nitrate Reduction to Nitrogen. *Angew. Chem., Int. Ed.* **2023**, *62*, No. e202217071.

(22) Wang, C.; Zhang, Y.; Luo, H.; Zhang, H.; Li, W.; Zhang, W.-X.; Yang, J. Iron-Based Nanocatalysts for Electrochemical Nitrate Reduction. *Small Methods* **2022**, *6*, 2200790.

(23) Zeng, Y.; Priest, C.; Wang, G.; Wu, G. Restoring the Nitrogen Cycle by Electrochemical Reduction of Nitrate: Progress and Prospects. *Small Methods* **2020**, *4*, 2000672.

(24) Khomutov, N.; Stamkulov, U. Nitrate Reduction at Various Metal Electrodes. *Sov. Electrochem.* **1971**, *7*, 312.

(25) Harris, L. The Lower Electronic States of Nitrite and Nitrate Ion, Nitromethane, Nitramide, Nitric Acid, and Nitrate Esters. *J. Chem. Phys.* **1973**, *58*, 5615.

(26) Hu, Q.; Qin, Y.; Wang, X.; Wang, Z.; Huang, X.; Zheng, H.; Gao, K.; Yang, H.; Zhang, P.; Shao, M.; et al. Reaction Intermediate-Mediated Electrocatalyst Synthesis favors Specified Facet and Defect Exposure for Efficient Nitrate-Ammonia Conversion. *Energy Environ. Sci.* **2021**, *14*, 4989−4997.

(27) Wang, J.; Feng, T.; Chen, J.; He, J.-H.; Fang, X. Flexible 2D Cu Metal: Organic Framework@MXene Film Electrode with Excellent

Durability for Highly Selective Electrocatalytic NH_3 Synthesis. *Research* **2022**, *2022*, 9837012.
(28) Song, Z.; Liu, Y.; Zhong, Y.; Guo, Q.; Zeng, J.; Geng, Z. Efficient Electroreduction of Nitrate into Ammonia at Ultralow Concentrations Via an Enrichment Effect. *Adv. Mater.* **2022**, *34*, 2204306.
(29) Liu, H.; Lang, X.; Zhu, C.; Timoshenko, J.; Rüscher, M.; Bai, L.; Guijarro, N.; Yin, H.; Peng, Y.; Li, J.; et al. Efficient Electrochemical Nitrate Reduction to Ammonia with Copper-Supported Rhodium Cluster and Single-Atom Catalysts. *Angew. Chem., Int. Ed.* **2022**, *61*, No. e202202556.
(30) He, W.; Zhang, J.; Dieckhöfer, S.; Varhade, S.; Brix, A. C.; Lielpetere, A.; Seisel, S.; Junqueira, J. R. C.; Schuhmann, W. Splicing the Active Phases of Copper/Cobalt-based Catalysts Achieves High-rate Tandem Electroreduction of Nitrate to Ammonia. *Nat. Commun.* **2022**, *13*, 1129.
(31) Zhu, T.; Chen, Q.; Liao, P.; Duan, W.; Liang, S.; Yan, Z.; Feng, C. Single-Atom Cu Catalysts for Enhanced Electrocatalytic Nitrate Reduction with Significant Alleviation of Nitrite Production. *Small* **2020**, *16*, 2004526.
(32) Wu, K.; Sun, C.; Wang, Z.; Song, Q.; Bai, X.; Yu, X.; Li, Q.; Wang, Z.; Zhang, H.; Zhang, J.; et al. Surface Reconstruction on Uniform Cu Nanodisks Boosted Electrochemical Nitrate Reduction to Ammonia. *ACS Mater. Lett.* **2022**, *4*, 650−656.
(33) Xu, Y.; Wang, M.; Ren, K.; Ren, T.; Liu, M.; Wang, Z.; Li, X.; Wang, L.; Wang, H. Atomic Defects in Pothole-rich Two-Dimensional Copper Nanoplates Triggering Enhanced Electrocatalytic Selective Nitrate-to-Ammonia Transformation. *J. Mater. Chem. A* **2021**, *9*, 16411−16417.
(34) Wu, T.; Kong, X.; Tong, S.; Chen, Y.; Liu, J.; Tang, Y.; Yang, X.; Chen, Y.; Wan, P. Self-Supported Cu Nanosheets Derived from CuCl-CuO for Highly Efficient Electrochemical Degradation of NO_3^-. *Appl. Surf. Sci.* **2019**, *489*, 321−329.
(35) Li, C.; Liu, S.; Xu, Y.; Ren, T.; Guo, Y.; Wang, Z.; Li, X.; Wang, L.; Wang, H. Controllable Reconstruction of Copper Nanowires into Nanotubes for Efficient Electrocatalytic Nitrate Conversion into Ammonia. *Nanoscale* **2022**, *14*, 12332−12338.
(36) Wang, Y.; Zhou, W.; Jia, R.; Yu, Y.; Zhang, B. Unveiling the Activity Origin of a Copper-based Electrocatalyst for Selective Nitrate Reduction to Ammonia. *Angew. Chem., Int. Ed.* **2020**, *59*, 5350−5354.
(37) Ren, T.; Ren, K.; Wang, M.; Liu, M.; Wang, Z.; Wang, H.; Li, X.; Wang, L.; Xu, Y. Concave-Convex Surface Oxide Layers over Copper Nanowires Boost Electrochemical Nitrate-to-Ammonia Conversion. *Chem. Eng. J.* **2021**, *426*, 130759.
(38) Yuan, J.; Xing, Z.; Tang, Y.; Liu, C. Tuning the Oxidation State of Cu Electrodes for Selective Electrosynthesis of Ammonia from Nitrate. *ACS Appl. Mater. Interfaces* **2021**, *13*, 52469−52478.
(39) Ren, Y.; Yu, C.; Wang, L.; Tan, X.; Wang, Z.; Wei, Q.; Zhang, Y.; Qiu, J. Microscopic-Level Insights into the Mechanism of Enhanced NH_3 Synthesis in Plasma-Enabled Cascade N_2 Oxidation−Electroreduction System. *J. Am. Chem. Soc.* **2022**, *144*, 10193−10200.
(40) Zhao, J.; Shen, Z.; Yu, J.; Guo, Y.; Mushtaq, M. A.; Ding, Y.; Song, Z.; Zhang, W.; Huang, X.; Li, Y.; et al. Constructing Cu-CuO Heterostructured Skin on Cu Cubes to Promote Electrocatalytic Ammonia Production from Nitrate Wastewater. *J. Hazard. Mater.* **2022**, *439*, 129653.
(41) Yang, J.; Qi, H.; Li, A.; Liu, X.; Yang, X.; Zhang, S.; Zhao, Q.; Jiang, Q.; Su, Y.; Zhang, L.; et al. Potential-Driven Restructuring of Cu Single Atoms to Nanoparticles for Boosting the Electrochemical Reduction of Nitrate to Ammonia. *J. Am. Chem. Soc.* **2022**, *144*, 12062−12071.
(42) Zhang, D.-F.; Zhang, H.; Guo, L.; Zheng, K.; Han, X.-D.; Zhang, Z. Delicate Control of Crystallographic Facet-Oriented Cu_2O Nanocrystals and the Correlated Adsorption Ability. *J. Mater. Chem.* **2009**, *19*, 5220−5225.
(43) Wang, J.; Yu, L.; Hu, L.; Chen, G.; Xin, H.; Feng, X. Ambient Ammonia Synthesis via Palladium-Catalyzed Electrohydrogenation of Dinitrogen at Low Overpotential. *Nat. Commun.* **2018**, *9*, 1795.
(44) Garcia-Segura, S.; Lanzarini-Lopes, M.; Hristovski, K.; Westerhoff, P. Electrocatalytic Reduction of Nitrate: Fundamentals to Full-Scale Water Treatment Applications. *Appl. Catal., B* **2018**, *236*, 546−568.
(45) Li, J.; Li, M.; An, N.; Zhang, S.; Song, Q.; Yang, Y.; Li, J.; Liu, X. Boosted Ammonium Production by Single Cobalt Atom Catalysts with High Faradic Efficiencies. *Proc. Natl. Acad. Sci. U.S.A.* **2022**, *119*, No. e2123450119.
(46) Jin, H.; Li, L.; Liu, X.; Tang, C.; Xu, W.; Chen, S.; Song, L.; Zheng, Y.; Qiao, S.-Z. Nitrogen Vacancies on 2D Layered W_2N_3: A Stable and Efficient Active Site for Nitrogen Reduction Reaction. *Adv. Mater.* **2019**, *31*, 1902709.
(47) Zhu, P.; Xia, C.; Liu, C.-Y.; Jiang, K.; Gao, G.; Zhang, X.; Xia, Y.; Lei, Y.; Alshareef, H. N.; Senftle, T. P.; et al. Direct and Continuous Generation of Pure Acetic Acid Solutions via Electrocatalytic Carbon Monoxide Reduction. *Proc. Natl. Acad. Sci. U.S.A.* **2021**, *118*, No. e2010868118.
(48) Fu, X.; Zhao, X.; Hu, X.; He, K.; Yu, Y.; Li, T.; Tu, Q.; Qian, X.; Yue, Q.; Wasielewski, M. R.; et al. Alternative Route for Electrochemical Ammonia Synthesis by Reduction of Nitrate on Copper Nanosheets. *Appl. Mater. Today* **2020**, *19*, 100620.
(49) Li, J.; Zhan, G.; Yang, J.; Quan, F.; Mao, C.; Liu, Y.; Wang, B.; Lei, F.; Li, L.; Chan, A. W. M.; et al. Efficient Ammonia Electrosynthesis from Nitrate on Strained Ruthenium Nanoclusters. *J. Am. Chem. Soc.* **2020**, *142*, 7036−7046.
(50) Wu, Z.-Z.; Zhang, X.-L.; Niu, Z.-Z.; Gao, F.-Y.; Yang, P.-P.; Chi, L.-P.; Shi, L.; Wei, W.-S.; Liu, R.; Chen, Z.; et al. Identification of Cu(100)/Cu(111) Interfaces as Superior Active Sites for CO Dimerization During CO_2 Electroreduction. *J. Am. Chem. Soc.* **2022**, *144*, 259−269.
(51) Lin, S.-C.; Chang, C.-C.; Chiu, S.-Y.; Pai, H.-T.; Liao, T.-Y.; Hsu, C.-S.; Chiang, W.-H.; Tsai, M.-K.; Chen, H. M. Operando Time-resolved X-ray Absorption Spectroscopy Reveals the Chemical Nature Enabling Highly Selective CO_2 Reduction. *Nat. Commun.* **2020**, *11*, 3525.
(52) Jeon, H. S.; Timoshenko, J.; Rettenmaier, C.; Herzog, A.; Yoon, A.; Chee, S. W.; Oener, S.; Hejral, U.; Haase, F. T.; Roldan Cuenya, B. Selectivity Control of Cu Nanocrystals in a Gas-Fed Flow Cell through CO_2 Pulsed Electroreduction. *J. Am. Chem. Soc.* **2021**, *143*, 7578−7587.
(53) Xu, L.; Ma, X.; Wu, L.; Tan, X.; Song, X.; Zhu, Q.; Chen, C.; Qian, Q.; Liu, Z.; Sun, X.; et al. In Situ Periodic Regeneration of Catalyst during CO_2 Electroreduction to C_{2+} Products. *Angew. Chem., Int. Ed.* **2022**, *61*, No. e202210375.
(54) Yao, Y.; Zhu, S.; Wang, H.; Li, H.; Shao, M. A Spectroscopic Study on the Nitrogen Electrochemical Reduction Reaction on Gold and Platinum Surfaces. *J. Am. Chem. Soc.* **2018**, *140*, 1496−1501.
(55) Pérez-Gallent, E.; Figueiredo, M. C.; Katsounaros, I.; Koper, M. T. M. Electrocatalytic Reduction of Nitrate on Copper Single Crystals in Acidic and Alkaline Solutions. *Electrochim. Acta* **2017**, *227*, 77−84.
(56) Zhang, N.; Shang, J.; Deng, X.; Cai, L.; Long, R.; Xiong, Y.; Chai, Y. Governing Interlayer Strain in Bismuth Nanocrystals for Efficient Ammonia Electrosynthesis from Nitrate Reduction. *ACS Nano* **2022**, *16*, 4795−4804.
(57) Liu, S.; Qian, T.; Wang, M.; Ji, H.; Shen, X.; Wang, C.; Yan, C. Proton-filtering Covalent Organic Frameworks with Superior Nitrogen Penetration Flux Promote Ambient Ammonia Synthesis. *Nat. Catal.* **2021**, *4*, 322−331.
(58) Liu, J.-X.; Richards, D.; Singh, N.; Goldsmith, B. R. Activity and Selectivity Trends in Electrocatalytic Nitrate Reduction on Transition Metals. *ACS Catal.* **2019**, *9*, 7052−7064.
(59) Butcher, D. P.; Gewirth, A. A. Nitrate Reduction Pathways on Cu Single Crystal Surfaces: Effect of Oxide and Cl^-. *Nano Energy* **2016**, *29*, 457−465.
(60) Hu, T.; Wang, C.; Wang, M.; Li, C. M.; Guo, C. Theoretical Insights into Superior Nitrate Reduction to Ammonia Performance of Copper Catalysts. *ACS Catal.* **2021**, *11*, 14417−14427.

https://doi.org/10.1021/acscatal.3c01315
ACS Catal. 2023, 13, 7529−7537